Chapter 17
THz Tomography

Takayuki Shibuya and Kodo Kawase

Abstract Terahertz and millimeter waves penetrate various dielectric materials, including plastics, ceramics, crystals, and colorants, allowing terahertz transmission images to be measured [1–5]. Many terahertz images have been recorded and used in various applications. However, these images are almost exclusively 2D, and transmission-mode measurement of such images is limited to thin samples, with the absorption of the sample averaged in the direction of the path of the terahertz beam. Tomographic images can be used to acquire 3D images in the terahertz frequency range, as in the photonic or X-ray regions of the electromagnetic spectrum. In this chapter, we introduce the principle of operation of two types of tomography system: computed tomography (CT) using millimeter to terahertz waves and time-of-flight (TOF) terahertz tomography. The THz-CT technique is similar to X-ray CT, however, it has the advantage that imaging of the internal structure of soft materials is comparatively easy. On the other hand, TOF tomography employs a THz pulse with a width of less than a picosecond, and depth resolution of tens of microns is possible. Additionally, it is possible to measure samples that are opaque in the visible region.

17.1 Computed Tomography Using THz and Millimeter Waves

Two-dimensional THz transmission images were first acquired by Hu and Nuss in 1995 [1]. Those images were of a semiconductor integrated circuit and of a leaf. The image of a freshly cut leaf was compared with that acquired after the leaf had

T. Shibuya
Tokyo Metropolitan Industrial Technology Research Institute, Tokyo, Japan
e-mail: shibuya.takayuki@iri-tokyo.jp

K. Kawase (✉)
Department of Electrical and Electronic Engineering and Information Engineering,
Graduate School of Engineering, Nagoya University, Nagoya464-8603, Japan
e-mail: kawase@nuee.nagoya-u.ac.jp

K.-E. Peiponen et al. (eds.), *Terahertz Spectroscopy and Imaging*,
Springer Series in Optical Sciences 171, DOI: 10.1007/978-3-642-29564-5_17,

been allowed to dry for 48 h, which revealed that transmission of THz radiation was much higher in the dry leaf, due to the decreased water content. Since then, various studies have demonstrated developments in THz imaging [2–5]. Two-dimensional transmission imaging measures the average absorption in the direction of the terahertz beam. However, it is often desirable to acquire 3D images. Computed tomography (CT) is a method that allows measurement of the internal structure of samples. CT has been developed primarily in the X-ray region, but it can also be applied to measurements using THz radiation. By using THz radiation, more sensitive measurements of soft materials can be expected compared to using X-rays, because of the reduced transmission at THz frequencies. However, because the THz radiation causes scattering and diffraction, unlike X-rays, there are some additional complications that must be taken into account.

17.1.1 Principle of CT

The filtered back projection (FBP) method [6] is one of the more frequently used CT techniques. First, the coordinate system of the xy plane, shown in Fig. 17.1, is defined, and the distribution of the extinction coefficient of the sample is assumed to be $f(x, y)$. Next, new orthogonalization coordinates of an XY plane, which is rotated by an angle θ around the origin, are defined. Electromagnetic radiation of intensity I_0 enters the sample parallel to the Y axis, and the transmitted intensity $I(X, \theta)$ is as follows:

$$I(X, \theta) = I_0 \exp[-\int_{-\infty}^{\infty} f(x, y)\mathrm{d}Y]. \tag{17.1}$$

$I(X, \theta)$ can be measured experimentally, and the absorbance $g(X, \theta)$ can be expressed as:

$$g(X, \theta) = \ln[\frac{I_0}{I(X, \theta)}] = \int_{-\infty}^{\infty} f(x, y)\mathrm{d}Y. \tag{17.2}$$

This technique for obtaining the projection data $g(X, \theta)$ associated with $f(x, y)$ is called Radon conversion. The purpose of CT is to calculate $f(x, y)$ from the experimentally measured $g(X, \theta)$. The 2D Fourier transformation of $f(x, y)$ is assumed to be of the form:

$$F(\xi, \eta) = \int_{-\infty}^{\infty}\int_{-\infty}^{\infty} f(x, y) \exp[-i(\xi x + \eta y)]\mathrm{d}x\mathrm{d}y, \tag{17.3}$$

where the coordinate system (ξ, η) is converted into a polar coordinate system (ω, θ), according to the following relations:

$$\begin{cases} \xi = \omega \cos\theta \\ \eta = \omega \sin\theta \end{cases}. \tag{17.4}$$

Following this transformation, Eq. (17.3) becomes:

$$F(\omega\cos\theta, \omega\sin\theta) = \int_{-\infty}^{\infty}\int_{-\infty}^{\infty} f(x, y)\exp[-i\omega(x\cos\theta + y\sin\theta)]\mathrm{d}x\mathrm{d}y. \tag{17.5}$$

Using the following relations,

$$\begin{aligned} &X = x\cos\theta + y\sin\theta, \\ &\mathrm{d}x\mathrm{d}y = \mathrm{d}X\mathrm{d}Y \end{aligned} \tag{17.6}$$

Equation (17.5) can be rewritten as

$$\begin{aligned} F(\omega\cos\theta, \omega\sin\theta) &= \int_{-\infty}^{\infty}\int_{-\infty}^{\infty} f(x, y)\exp(-i\omega X)\mathrm{d}X\mathrm{d}Y \\ &= \int_{-\infty}^{\infty}\int_{-\infty}^{\infty} [f(x, y)\mathrm{d}Y]\exp(-i\omega X)\mathrm{d}X \\ &= \int_{-\infty}^{\infty} g(X, \theta)\exp(-i\omega X)\mathrm{d}X \end{aligned} \tag{17.7}$$

$F(\xi, \eta)$ is the two-dimensional Fourier transform of $f(x, y)$, and so $f(x, y)$ can be determined from $g(X, \theta)$, which is obtained in the range $0 \leqq \theta < \pi$. Thus, $f(x, y)$ is related to $F(\xi, \eta)$ as follows:

$$f(x, y) = \frac{1}{(2\pi)^2}\int_{-\infty}^{\infty}\int_{-\infty}^{\infty} F(\xi, \eta)\exp[i(\xi x + \eta y)]\mathrm{d}\xi\mathrm{d}\eta. \tag{17.8}$$

Equation (17.8) can be converted to a polar coordinate system by using Eq. (17.4), resulting in:

$$f(x, y) = \frac{1}{(2\pi)^2}\int_{0}^{2\pi}\int_{0}^{\infty} F(\omega\cos\theta, \omega\sin\theta)\exp[i\omega(x\cos\theta + y\sin\theta)]\omega\mathrm{d}\omega\mathrm{d}\theta. \tag{17.9}$$

To enhance the range of ω in the negative region, the absolute value, $|\omega|$, is taken in Eq. (17.9), so that we have:

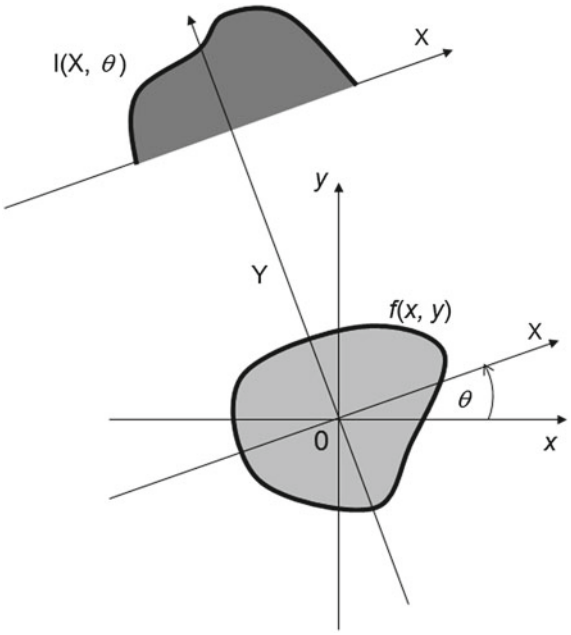

Fig. 17.1 Schematic illustration of radon conversion, and the sample coordinate system

$$f(x, y) = \frac{1}{2(2\pi)^2} \int_0^{2\pi} [\int_{-\infty}^{\infty} F(\omega \cos\theta, \omega \sin\theta) \exp(i\omega X)\, |\omega| \mathrm{d}\omega] \mathrm{d}\theta. \tag{17.10}$$

Using the following relationship,

$$\begin{aligned} q(X, \theta) &= \frac{1}{2\pi} \int_{-\infty}^{\infty} F(\omega \cos\theta, \omega \sin\theta) \exp(i\omega X)\, |\omega| \mathrm{d}\omega \\ &= \frac{1}{2\pi} \int_{-\infty}^{\infty} [\int_{-\infty}^{\infty} g(X, \theta) \exp(-i\omega X)]\, |\omega| \exp(i\omega X) \mathrm{d}\omega, \end{aligned} \tag{17.11}$$

$f(x, y)$ can be expressed as follows:

$$f(x, y) = \frac{1}{4\pi} \int_0^{2\pi} q(X, \theta) \mathrm{d}\theta. \tag{17.12}$$

From Eq. (17.11) it follows that $q(X, \theta)$ can be obtained by the inverse Fourier transform of $F(\omega \cos\theta, \omega \sin\theta)$, that is, the Fourier transform of $g(X, \theta)$ after the

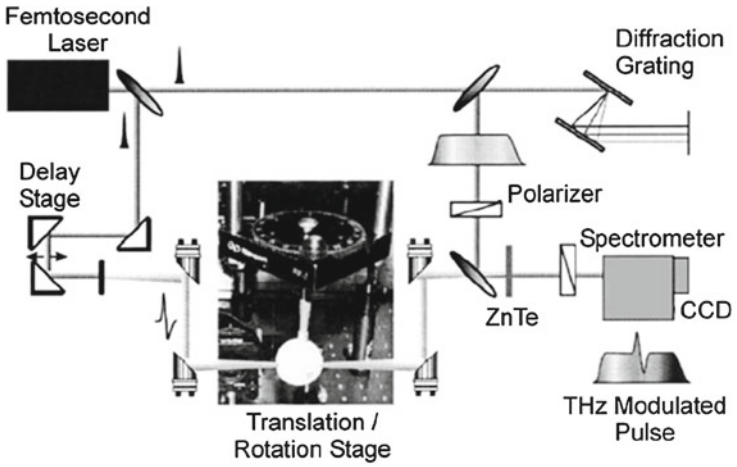

Fig. 17.2 Experimental setup for CT imaging using a THz-TDS system

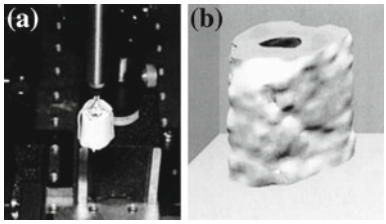

Fig. 17.3 **a** Optical image of a turkey-bone sample and **b** reconstructed 3D image of the sample measured using THz-TDS CT

filtering process using $|\omega|$. Therefore, $f(x, y)$ can be calculated according to the back-projection process of $q(X, \theta)$, shown in expression (17.12).

17.1.2 Examples of the Application of THz-CT

Ferguson et al. first demonstrated THz-CT [7], using a transmission THz-TDS system. Figure 17.2 shows the experimental setup used for THz-CT. The sample is arranged in the optical path of the THz pulse, and the projection image is acquired by scanning the sample using translation/rotation stages. Figure 17.3a shows an optical image of a section of turkey bone, and Fig. 17.3b shows the THz-CT image of the same sample. Both the central cavity of the bone and the outline can be clearly observed.

In recent years, air pollution due to emissions from internal combustion engines has become a significant problem. In particular, soot particulates from vehicle emissions, of which the principal ingredient is carbon, are harmful to human health. Thus, soot-removal filters installed in the exhaust system can reduce these particulate

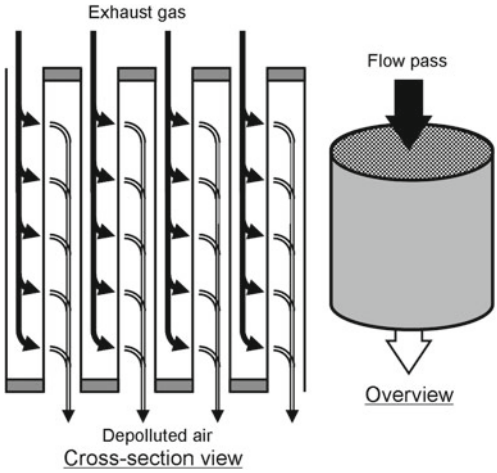

Fig. 17.4 Internal view (*left*) and overview (*right*) of a soot-removal filter. The exhaust gas is filtered by passing it through 0.4 mm-thick ceramic walls

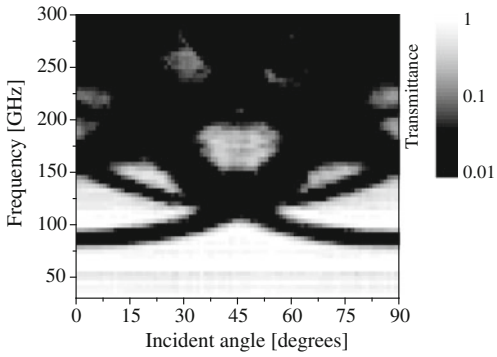

Fig. 17.5 Transmittance mapping as a function of the angle of incidence and frequency; the transmittance is indicated in a pseudo-color plot

emissions. Measurement of the distribution of soot in a soot-removal filter was reported in 2010 as another example of THz/MMW CT [8]. Figure 17.4 shows a schematic diagram of the filter. The exhaust gas is filtered by passing through ceramic walls, and is discharged into the atmosphere. The development of a filter with high soot-trapping efficiency is difficult, because it is hard to characterize the distribution of soot in the filter since that requires dismantling or destroying it. Therefore, a non-destructive technique for measuring the distribution of accumulated soot is desirable.

To construct a tomographic image, it is necessary to measure the transmittance of the filter from all azimuthal angles. Transmittance mapping as a function of the angle of incidence and frequency is shown in Fig. 17.5. The dependence of the transmittance on the angle of incidence is shown in Fig. 17.6 at 65, 80, 150, 175, and 250 GHz. The transmittance is strongly dependent on the angle of incidence at the higher frequencies, resulting in behavior that is similar to that observed in photonic crystals, with pronounced dips. These dips in the transmittance are caused by photonic band

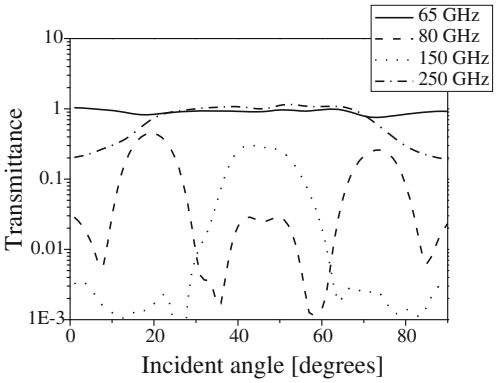

Fig. 17.6 Transmittance as a function of the angle of incidence at several frequencies. Strong dips in the transmittance are seen at higher frequencies

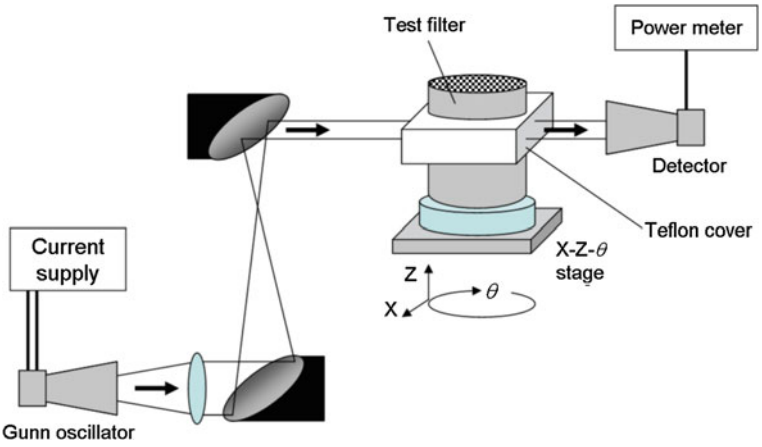

Fig. 17.7 Schematic diagram of the 3D-CT image-acquisition system

gaps in the periodic filter structure, whereas transmittance is almost flat at 65 GHz. Thus, 65 GHz was chosen as the operating frequency of the CT system, so that the position of the soot deposits could be determined without artifacts from the structure of the filter affecting the image.

A schematic diagram of the CT imaging system is shown in Fig. 17.7. A 65 GHz Gunn oscillator was employed as the source, and the output was collimated using a horn antenna and a dielectric lens. The beam diameter was reduced using two parabolic mirrors, to a full-width at half-maximum beam of 9.4 mm, and the sample was placed on an X-Z-θ stage in the path of the collimated beam. Since the sample was cylindrical, it behaved as a rod lens, and so it was enclosed within a Teflon cover to prevent refraction at the sample/air interface. As shown in Fig. 17.8, a test filter with a non-uniform distribution of soot was used. A reconstructed 3D image obtained using a FBP method is shown in Fig. 17.9. The regions of accumulated soot can clearly be seen. Some loss of resolution and distortion of the image occurs

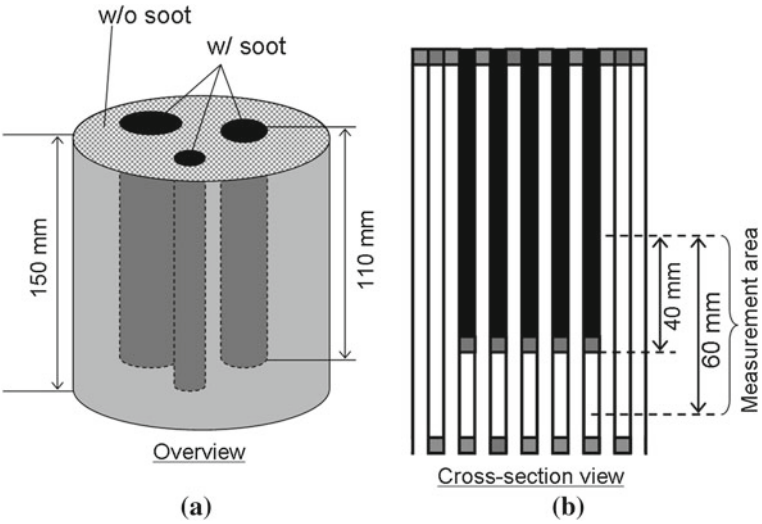

Fig. 17.8 Schematic diagram of the test sample of the soot-removal filter. **a** Soot is located in the three 110 mm-long cylindrical regions shown in black. The density of the soot is 4.7 g/L. The final 40 mm of the filter does not contain any soot. **b** Microstructure of the sample soot-removal filter. The soot is located in the inlet regions of the filter, as shown by the black sections, and the sooty regions terminate part way along the length of the filter. The 60 mm-long measurement region is illustrated

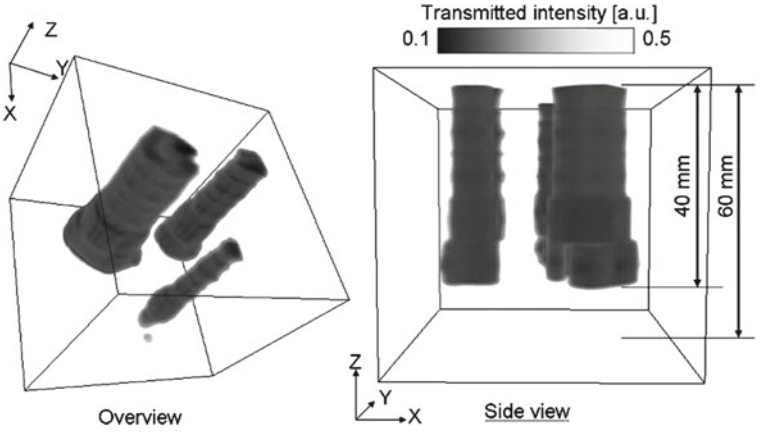

Fig. 17.9 The 3D-CT reconstructed image of the soot-removal filter

because of diffraction due to the mismatch of the refractive indices of the filter and the Teflon cover, and due to artifacts of the Fourier transform.

17.2 Time-of-Flight Terahertz Tomography

Time-of-flight terahertz (TOF-THz) tomography is based on a reflection-type THz-TDS system. Since the electromagnetic field in sub-picosecond terahertz pulses is measured directly using THz-TDS, the multilayered structure of a sample can be imaged by detecting the pulses reflected from the interfaces between layers. This technique is valuable in industry because the unique transmission characteristics of terahertz radiation enable inspection of multilayered paints in industrial products or tablet coatings [9, 10], which cannot be measured using optical coherence tomography (OCT) based on an optical light source [11].

17.2.1 Principle of TOF Tomography

The setup of a TOF-THz tomography system is illustrated in Fig. 17.10. If the sample has a multilayered structure, such as is shown in Fig. 17.10, the pulse is partially reflected because of the discontinuity in the refractive index at each interface, and details of the multilayer structure can be inferred from the reflected pulse train. If we assume that the THz pulse is normally incident on the sample, the delay Δt of the reflected pulse is determined from:

$$\Delta t = \frac{2n_g d}{c}, \tag{17.13}$$

where n_g, d, c are the refractive index, the thickness of each layer, and the speed of light, respectively. If the refractive index of the layers is known, d can be determined as follows by measuring the delay time of each pulse, i.e.,

$$d = \frac{c\Delta t}{2n_g}. \tag{17.14}$$

This can readily be extended to samples where the THz pulse is incident on the sample at an angle θ, as follows

$$d = \frac{c\Delta t}{2n_g}\cos\theta. \tag{17.15}$$

The resolution depends on the width of the incident THz pulse, and is improved when the pulse is short. When the THz pulse is not ideal (e.g., a top-hat function), but varies with time in some anolomous manner, distinction of the reflected pulse becomes difficult, and ghost interfaces can appear in the tomographic image. These ghost images can be eliminated using signal processing, for example by employing deconvolution algorithms.

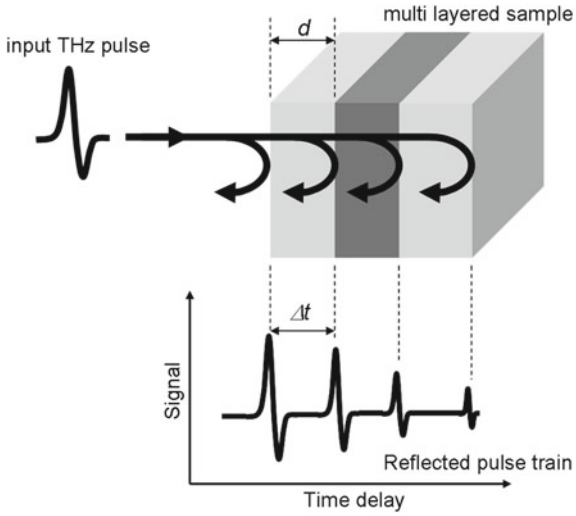

Fig. 17.10 Principle of TOF-THz tomography

Wiener deconvolution is typically used in tomographic sensing. The time variation of the reference, $x(t)$, and sample, $y(t)$, are assumed to be known. Here, $x(t)$ is the waveform of the THz pulse in the THz-TDS system, and $y(t)$ can be found by convolving this with the transfer function $h(t)$, where $h(t)$ is determined by the multilayer film structure of the sample, i.e.,

$$y(t) = \int_{-\infty}^{\infty} h(\tau)x(t-\tau)\mathrm{d}\tau = h(t)*x(t). \tag{17.16}$$

This can be rewritten in the frequency domain as:

$$Y(\omega) = H(\omega) \cdot X(\omega). \tag{17.17}$$

The inverse Fourier transformation of $H(\omega)$ is as follows:

$$h(t) = \Im^{-1}\left\{Y(\omega) \cdot \frac{1}{X(\omega)}\right\}, \tag{17.18}$$

so that information on the structure of the sample, i.e., $h(t)$, can be obtained. Here, the Wiener filter is used so that the right-hand side of the expression (17.18) may diverge when a value with very small value of $X(\omega)$ is obtained. The Wiener filter, $W(\omega)$, is defined as:

$$W(\omega) = \frac{\overline{X}(\omega)}{|X(\omega)|^2 + 1/a}, \tag{17.19}$$

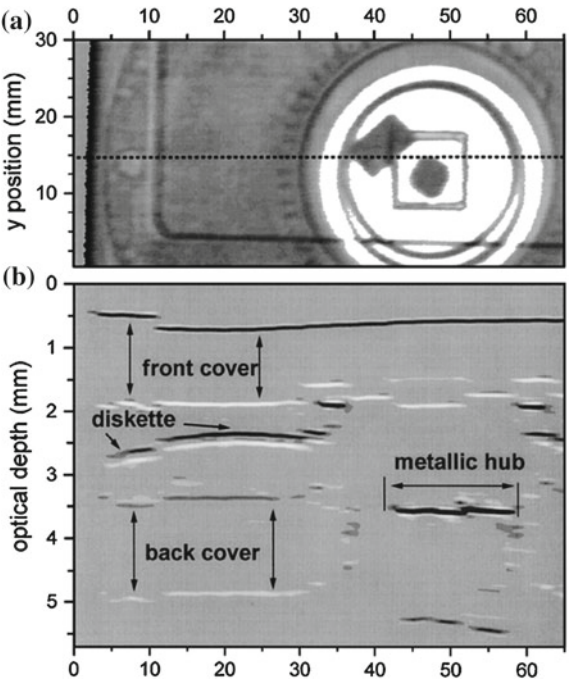

Fig. 17.11 **a** Conventional reflective THz image of a 3.5 in. floppy disk. **b** Tomographic image of the same floppy disk at a constant vertical position, indicated by the dashed line at $y = 15\,\text{mm}$ in **a**

where the term a is the ratio of the original function to noise. The Wiener filter modifies expression (17.18) so that we have:

$$h(t) = \Im^{-1}\left\{ Y(\omega) \cdot \frac{1}{W(\omega)} \right\}. \tag{17.20}$$

Additional artifacts of the THz pulse can be removed by using windowing, further improving the ability to correctly detect interfaces.

17.2.2 Examples of TOF-THz Tomography

In 1997, Mittleman et al. used TOF tomography to obtain a tomographic image of a floppy disk, and compared it with a conventional THz 2D image [12]. Figure 17.11a shows a conventional THz reflective image, and Fig. 17.11b shows a tomographic image of the same sample. The internal structures are visible in the tomographic image, including the cover, diskette, and metallic hub. The tomographic image in Fig. 17.11a is composed of an array of time-delayed pulses along the line $y = 15$. Figure 17.12b shows the raw reflected-waveform data from a single point in the image. It is not easy to distinguish each interface in the reflected pulse train, because

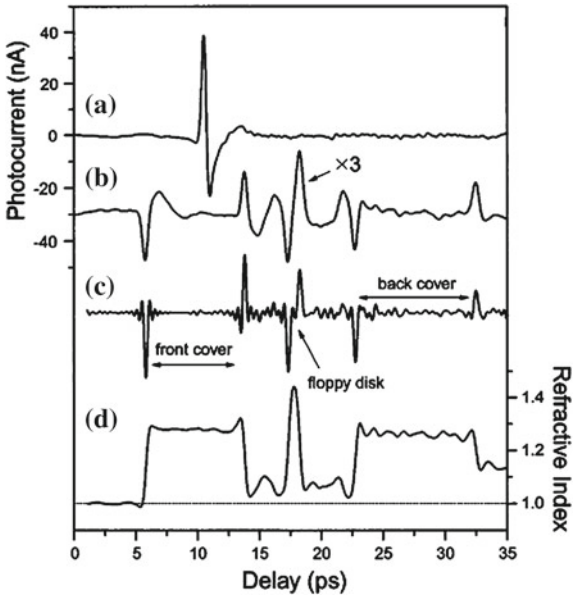

Fig. 17.12 **a** The THz pulse. **b** The reflected waveform from a single point on the 3.5 in. floppy disk. The *curve* shown in **c** is the reflected waveform after signal processing. *Curve* **d** is the refractive index profile of the medium (*right-hand axis*), derived from curve **c** using Eqs. (17.3) and (17.4)

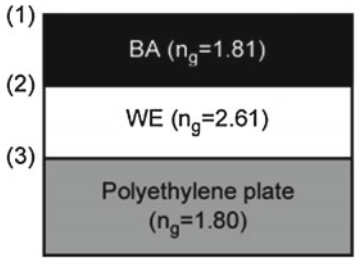

Fig. 17.13 The layer structure of the sample

of the form of the THz pulse. Figure 17.12c shows the reflected pulse train after deconvolution and filtering. The location of the interfaces is much easier to detect in the processed signal. The positive features in the processed waveform correspond to interfaces where the THz beam transitioned from a high-refractive-index medium to a lower refractive index medium, and vice versa for the negative features.

In 2005, Yasui et al. demonstrated tomographic imaging of paint on car body panels using TOF-THz tomography [13]. It is difficult to determine the thickness of each layer using conventional methods. The measured sample is a two-layer paint film, as illustrated in Fig. 17.13. Black acrylic (BA) and white enamel (WE) paints were layered on a polyethylene substrate. The group refractive indexes of BA, WE, and polyethylene are 1.81, 2.61, and 1.80 respectively. Figure 17.15 shows the impulse response signal of the reflected THz pulse train at a single point in the two-layer paint film, where numerical Fourier deconvolution was used to improve the detection of the interfaces. The first two (positive) pulses correspond to the air–BA

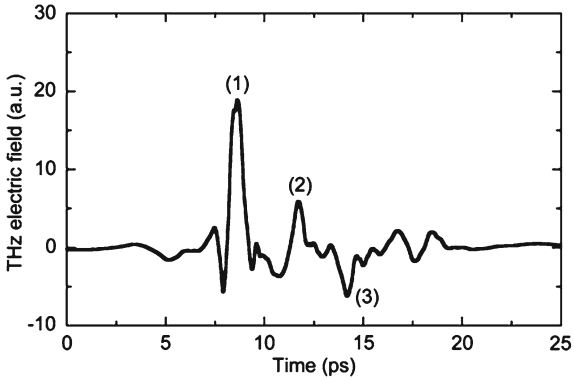

Fig. 17.14 The THz signal reflected from a single point on the sample. The numbers correspond to the location of the interfaces in the multilayer structure

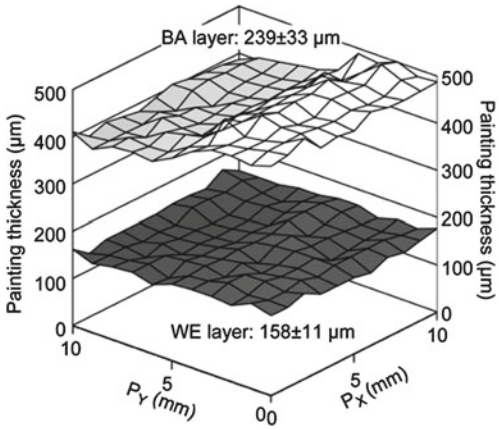

Fig. 17.15 Spatial distribution of the interfaces in a multilayer paint film on a dielectric substrate

and BA–WE boundaries, and the third (negative) pulse corresponds to the WE-substrate boundary. Figure 17.15 shows the spatial variation of the location of the interfaces in the paint film, calculated from the time delay and the group refractive index.

Yasui et al. demonstrated monitoring of the drying process of a single-layer film. As a process to control paint quality, monitoring of paint drying is often required in addition to measurement of the final thickness. The shape of the reflected pulse train will change depending on the dryness of the sample if the refractive index or absorption coefficient of the sample varies depending on whether the paint is wet or dry. Figure 17.16 shows the reflected pulse train from the sample before and after painting. Only one pulse from the air–substrate boundary is observed before painting, while two pulses, from the air–BA and BA–substrate boundaries, appear after painting. The difference in the delay time between the two reflected pulses shortened as the paint dried, and it can be seen that the drying process finished after about 10 min.

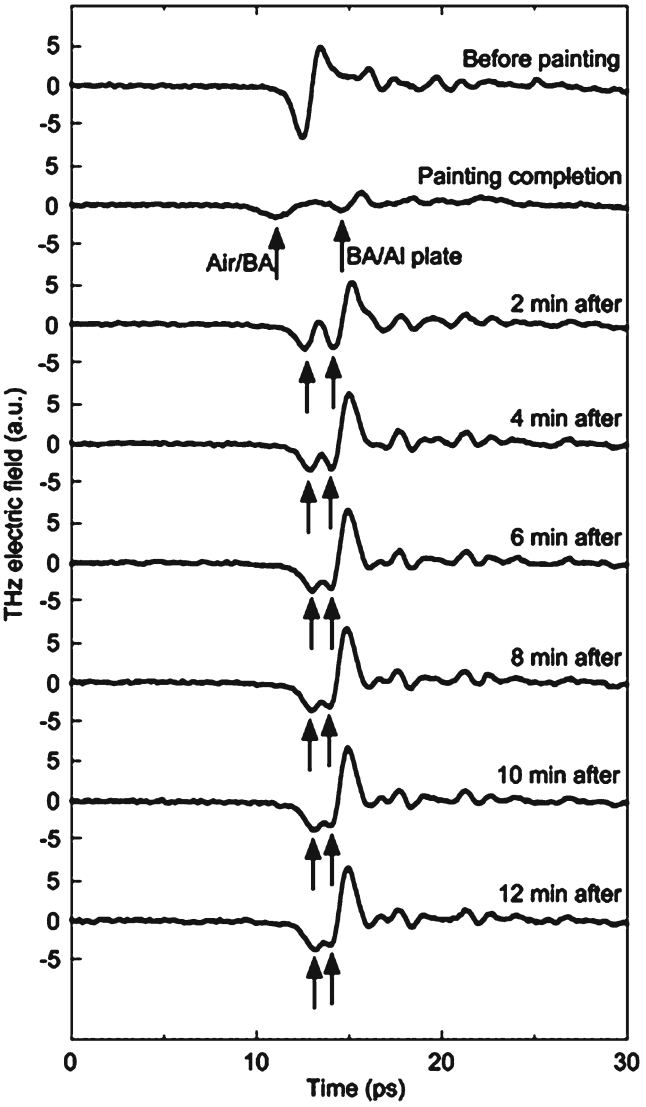

Fig. 17.16 Evolution of a reflected THz pulse train before and after painting. No change in the signal is seen after 10 min, indicating that the paint has dried

Improvement in depth resolution, output power, and robustness, as well as a reduction in the size of the system, are required for industrial applications. Takayanagi et al. developed a TOF tomography system with improved depth resolution using a femtosecond fiber laser system for the pump source [14]. They developed an all-fiber laser system that produced 17 fs optical pulses at a wavelength of 1.56 μm,

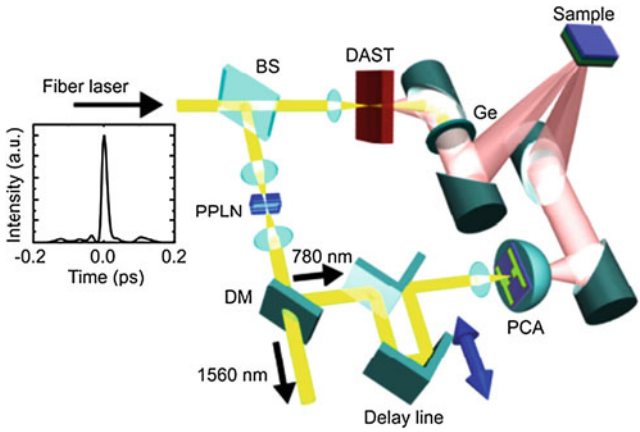

Fig. 17.17 Experimental setup of a high-resolution TOF-THz tomography system using a fiber laser. The inset shows the waveform of the 17 fs fiber laser. *BS* beam splitter; *PPLN* periodically poled lithium niobate; *DM* dichroic mirror; *PCA* photoconductive antenna; *Ge* germanium plate

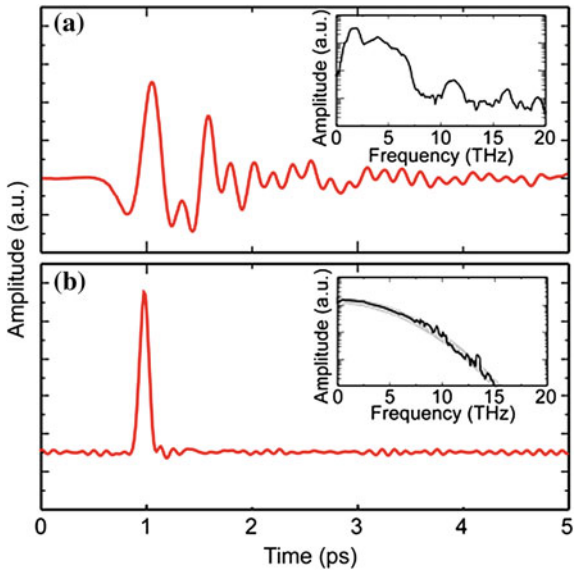

Fig. 17.18 The reflected THz pulse raw data (**a**) and after signal processing (**b**). The insets show the corresponding Fourier transforms. The *gray curve* in the inset of (**b**) shows the Fourier transform of a Gaussian pulse

and generated and detected broadband terahertz pulses ranging from 0.1 to 27 THz. Their experimental TOF-THz tomography setup is shown in Fig. 17.17; the insert shows the compressed optical pulses. The average power of the pulses was 200 mW, and the repetition rate was 48 MHz.

Figure 17.18a shows the reflected THz signal when an aluminum plate was placed at the sample position. The maximum amplitude is at around 1 ps, with further oscillating components for a few picoseconds afterwards, due to a peculiar

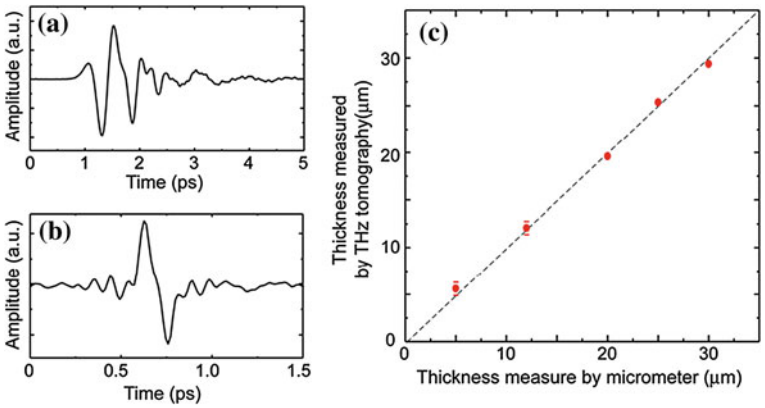

Fig. 17.19 Evaluation of axial resolution using Teflon films. **a** Typical measured reflected pulse, **b** the reflected pulse after signal processing, and **c** the thickness of the Teflon films measured with TOF-THz as a function of thickness measured using a micrometer

absorption characteristic of DAST crystal. This anomalous reflected waveform makes it more difficult to detect interfaces as compared with THz pulse generation using a photoconductive antenna, and signal processing is required to improve the data. Figure 17.18b shows a processed waveform using the data shown in Fig. 17.18a, which has a single peak.

Figure 17.19 shows the TOF-THz data for a Teflon film of varying thickness. Teflon membranes of thickness 5, 12, 20, 25, and 30 microns were used for the measurements. Figure 17.19a and b are reflected THz pulses before and after signal processing from the 12 μm-thick Teflon film. The two interfaces defining the film can be clearly observed in the processed signal. Figure 17.19c shows tomographic measurements of the thickness of the Teflon films. The depth resolution of this system is better than $10/n$ microns, where $n = 1.9$ is the refractive index of the Teflon membrane. It is anticipated that this technology will lead to the development of systems capable of inspecting the thickness of thin films in applications such as inspecting paint, human skin, and the peel of farm fruit and vegetable products.

References

1. B. Hu, M. Nuss, Opt. Lett. **20**, 1716 (1995)
2. D. Mittleman, M. Gupta, R. Neelamani, R. Baraniuk, J. Rudd, M. Koch, Appl. Phys. B Laser Opt. **68**, 1085 (1999)
3. R. Woodward, B. Cole, V. Wallace, R. Pye, D. Arnone, E. Linfield, M. Pepper, Phys. Med. Biol. **47**, 3853 (2002)
4. K. Kawase, Y. Ogawa, Y. Watanabe, H. Inoue, Opt. Express **11**, 2549 (2003)
5. A. Dobroiu, M. Yamashita, Y. Ohshima, C. Otani, K. Kawase, Appl. Opt. **43**, 5637 (2004)
6. G.T. Herman, *Image Reconstruction from Projections–The Fundamentals of Computerized Tomography* (Academic, New York, 1980)

7. B. Ferguson, S. Wang, D. Gray, D. Abbot, X.C. Zhang, Opt. Lett. **27**, 1312 (2002)
8. T. Shibuya, T. Suzuki, K. Suizu, K. Kawase, J. Infrared Millim. THz waves. doi:10.1007/s10762-010-9672-6
9. H. Zhao, X. Guang, J. Huang, Phys. E **40**, 3025 (2008)
10. B. Wang, G. Wang, Appl. Phys. Lett. **87**, 013107 (2005)
11. W. Lin, G. Wang, Appl. Phys. Lett. **91**, 143121 (2007)
12. D. Mittleman, S. Hunsche, L. Boivin, M. Nuss, Opt. Lett. **22**, 904 (1997)
13. T. Yasui, T. Yasuda, K. Sawanaka, T. Araki, Appl. Opt. **44**, 6849 (2005)
14. J. Takayanagi, H. Jinno, S. Ichino, K. Suizu, M. Yamashita, T. Ouchi, S. Kasai, H. Ohtake, H. Uchida, N. Nishizawa, K. Kawase, Opt. Express **17**, 7549 (2009)